ADVANCED FUNCTIONAL MATERIALS
www.afm-journal.de

Interface Polarization Strengthened Microwave Catalysis of MoS_2/FeS/Rhein for the Therapy of Bacteria-Infected Osteomyelitis

*Liguo Jin, Xiangmei Liu, Yufeng Zheng, Zhaoyang Li, Yu Zhang, Shengli Zhu, Hui Jiang, Zhenduo Cui, Paul K. Chu, and Shuilin Wu**

Staphylococcus aureus (_S. aureus_)-induced osteomyelitis is fatal to patients, even leading to death without timely debridement processing, which is difficult to be treated by antibiotics or phototherapy due to deep infections. Herein, a microwave (MW) assisted bacteria-killing strategy for treating _S. aureus_-induced osteomyelitis by using MW-responsive molybdenum disulfide (MoS_2)/ferrous sulfide (FeS) heterojunction with anti-inflammatory herb of rhein (Rhe) is reported. Under medical MW irradiation, MoS_2/FeS/Rhe effectively eradicates _S. aureus_-infected rat tibial osteomyelitis. The robust therapeutic effects of MoS_2/FeS/Rhe are ascribed to the anti-inflammatory effect of Rhe, the enhanced MW thermal and dynamic effects of MoS_2/FeS. MoS_2/FeS is composed of S-Mo-S-Fe-S stacked layers sandwiched in between by weak Van Der Waals interactions, which means that ions or molecules can be retained in the space between the layers. Under MW irradiation, dipoles or ions are aligned in an oscillating electric field, which cause dipolar polarization and ionic conduction, leading to molecular friction and dielectric loss to generate MW heat. In addition, the dipole orientation polarization caused by the interfacial polarization of MoS_2/FeS is the main factor for microwave catalysis. This kind of MW responsive nanocomposite comprising inorganics and herbs may solve the challenge of how to effectively treat deep tissue infections.

1. Introduction

Osteomyelitis is a serious bone-destroying-induced deep inflammation disease infected by bacterial infections,[1] which has a high incidence, with recurrent and persistent infections occurring in ≈40% patients.[2] This kind of deep tissue infection may often lead to abscesses, organ infections, and sepsis.[3–6] Clinically, *Staphylococcus aureus* (*S. aureus*) is the main pathogen causing osteomyelitis, which invades normal cells to induce apoptosis, and also produces toxins to destroy local tissues.[7] At present, osteomyelitis is usually treated with multiple surgical debridements and systemic injections of large amounts of antibiotics, which generally requires a long treatment time.[8] Overuse of antibiotics has been reported to lead to bacterial resistance to antibiotics. Large dosage of antibiotics can also damage the innate immune system and cause serious adverse effects.[9] In response to the antibiotic resistance crisis, antibiotic-free strategies have been emerging including photothermal therapy (PTT) and photodynamic therapy (PDT).[10] However, due to the poor penetration depth of near-infrared (NIR) light, both PTT and PDT are only suitable for treating epidermal tissue infection.[11] Therefore, there is an urgent need to develop effective therapeutic approaches to effectively cure deep tissue infections.

Medical microwave (MW), as a type of electromagnetic spectrum with long wave length, has deep penetration ability and negligible side effects, which may be a safe and effective therapeutic tool.[4,5,12,13] Recent studies have shown that MW thermosensitive agents can kill bacteria under MW irradiation.[4,5] However, the higher temperature and longer treatment time will inevitably scald normal tissues, so it is difficult to directly

L. Jin, Z. Li, S. Zhu, H. Jiang, Z. Cui, S. Wu
School of Materials Science & Engineering, the Key Laboratory of Advanced Ceramics and Machining Technology by the Ministry of Education of China
Tianjin University
Yaguan Road 135#, Tianjin 300072, China
L. Jin, Y. Zheng, S. Wu
School of Materials Science & Engineering
Peking University
Yiheyuan Road 5#, Beijing 100871, China
E-mail: slwu@pku.edu.cn
The ORCID identification number(s) for the author(s) of this article can be found under https://doi.org/10.1002/adfm.202204437.
X. Liu
School of Life Science and Health Engineering
Hebei University of Technology
Xiping Avenue 5340#, Tianjin 300401, China
Y. Zheng, Y. Zhang
Department of Orthopedics
Guangdong Provincial People's Hospital
Guangdong Academy of Medical Sciences
Zhongshan 2nd Road 106#, Guangzhou 510080, China
P. K. Chu
Department of Physics, Department of Materials Science and Engineering, and Department of Biomedical Engineering
City University of Hong Kong
Tat Chee Avenue, Kowloon, Hong Kong 999077, China

DOI: 10.1002/adfm.202204437

treat bacterial infections by using MW heat at higher temperatures.[3] Previous study shows that radical oxygen species (ROS) can assist thermal effect to kill bacteria at a moderate temperature without scalding surrounding tissues.[14] Therefore, MW thermal therapy (MTT) combined with MW dynamic therapy (MDT) may be a promising option for treating bacterial infections effectively. It is necessary to develop biocompatible materials that can not only achieve enhanced MW thermal effect but also generate ROS. At present, the materials that can absorb MW mainly include magnetic loss materials and dielectric loss materials. The MW absorption performance can be enhanced by adjusting the impedance matching and attenuation constant between the dielectric materials.[15] Molybdenum disulfide (MoS_2) is a well-defined layered material consisting of stacked S-Mo-S layers sandwiched in the middle by weak Van Der Waals interactions, which means that ions or molecules can be retained in the space between the layers.[16] MoS_2 can cause dipole polarization and ion conduction under MW radiation, resulting in molecular friction and dielectric loss to generate MW heat.[13,17–19] The defective dipole polarization caused by Mo and S vacancies in MoS_2 is considered to be the main reason for achieving electromagnetic wave loss, but its inherent weak conductivity and few polarization active sites limits its application in the field of microwave absorption.[18,20,21] To address these issues, efforts have been made to improve the structural of MoS_2, including through interface construction, development of novel nanostructures, or hierarchical structural designs for impedance optimization.[20] As basic building blocks, MoS_2 combined with various components of dielectric or magnetic types for the construction of MoS_2-based absorbers such as MoS_2/rGO,[22] MoS_2@C,[23] and MoS_2/Fe_3O_4,[24] have been considered as typical strategies and have shown great potential for improving microwave absorption performance. Ferrous sulfide (FeS) has a bulky structure with a large specific surface area, and it is easy to adsorb polar molecules such as oxygen on the surface.[25] Therefore, the combination of MoS_2 and FeS may possess MW heat and generate ROS due to the possible interfacial polarization caused by sufficient interfacial interactions, which made this material be promising high-performance MTT or MDT reagent.[17,18] Even so, the in vivo application of hybrid nanomaterial must face the rejection reaction from the immune system, which may cause severe immunizing inflammatory reaction.[3] Therefore, anti-inflammatory is also a major concern in the treatment of osteomyelitis. Natural herbal medicines such as rhein, berberine, curcumin, and puerarin, are promising for treating inflammation.[26,27] Specifically, as we known, as a traditional Chinese herbal medicine, rhein (Rhe) is a free anthraquinone substance derived from the rhubarb, which has anti-inflammatory, antiviral, antioxidative, and renal function regulation effects. This kind of herb is widely distributed in the rhizomes of the olygonaceae plant Rheumpalmatum L., the roots of Polygonum multiflorum Thunb., and the pods of the legume Cassiaangustifolia Vahl.

Given this background, we proposed a MW-assisted therapeutic strategy for treating *S. aureus*-infected osteomyelitis by developing a MW-responsive nanocomposite of MoS_2/FeS modified by Rhe (**Figure 1**). The prepared MoS_2/FeS/Rhe nanocomposite exhibited highly effective antibacterial efficacy and anti-inflammatory effect, which was attributed to the MW-triggered thermal effect and ROS as well as anti-inflammatory activity of Rhe. The strong MW absorption capacity of MoS_2/FeS mainly came from the dielectric loss of reflection loss while its enhanced MW catalysis was attributed to its stronger oxygen (O_2) fixation ability than MoS_2 alone, which provided more O_2 source to capture electromagnetic hotspots. Additionally, more electromagnetic hotspots were generated at MoS_2/FeS interface than MoS_2 under MW irradiation due to interface polarization. Because of these induced electromagnetic hotspots, sodium species was field-ionized and subsequently reacted with oxygen to produce ROS ($^1O_2$ and $\cdot O_2^-$).

2. Results

2.1. Preparation and Characterization of MoS_2/FeS/Rhe

Scanning electron microscopy (SEM) images, elemental mapping and transmission electron microscopy (TEM) images all showed that the synthesized MoS_2 exhibited nanoflower-like structure (Figure S1, Supporting Information and **Figure 2**a). MoS_2/FeS was prepared using a one-pot solvothermal method. In this process, MoS_2 nanoflowers were uniformly dispersed, and FeS was formed in situ by reducing $FeCl_3$ in the hydrothermal reaction, thereby preparing MoS_2/FeS (Figure 2b and Figure S2, Supporting Information). High-resolution TEM (HRTEM) image showed the lattice spacing of 0.26 and 0.62 nm, corresponding to the (100) and (002) plane, respectively, indicating the successful synthesis of MoS_2. When recombined with FeS, the HRTEM images showed the lattice spacing of 0.25 nm, corresponding to the (201) plane, indicating the successful preparation of MoS_2/FeS with an obvious interface between them (marked by yellow line in Figure 2c,d). The tight interface between MoS_2 and FeS was beneficial to improve the MW absorption performance due to multiple reflections. SEM images, and elemental mapping showed that the Rhe exhibited organic crystal structure (Figure S3, Supporting Information). The composition of MoS_2/FeS/Rhe with Mo, S, Fe, and O elements was synergistically confirmed by TEM images and elemental mapping (Figure 2e). X-ray photoelectron spectroscopy (XPS) disclosed the existence of Mo, S, and Fe elements in the composites of MoS_2/FeS (Figure 2f). As shown in Figure 2g, MoS_2, FeS, and MoS_2/FeS had the corresponding peak position by X-ray diffraction (XRD) patterns, indicating the successful combination of MoS_2 and FeS. The ultra-violet and visible light (UV–vis) diffuse reflectance spectroscopy was performed to calculate the band gaps of MoS_2 and FeS, and the corresponding value was 1.19 and 2.09 eV, respectively (Figure S4a, Supporting Information). Meanwhile, the weight loss rates of MoS_2 and MoS_2/FeS were −19.25% and −47.31%, respectively by thermogravimetric (TG) curves, indicating the successful combination of MoS_2 and FeS (Figure 2h). Additionally, it could be found from the nitrogen adsorption–desorption curve shown in Figure 2i that MoS_2/FeS exhibited much higher gas adsorption capacity than MoS_2. The Raman spectra showed the peaks at 810 and 790 cm^{-1} of MoS_2/FeS compared with 810 cm^{-1} of MoS_2, indicating that MoS_2 and FeS were successfully recombined (Figure S4b, Supporting Information). The zeta potential measurements shown in Figure 2j, MoS_2 was negatively charged,

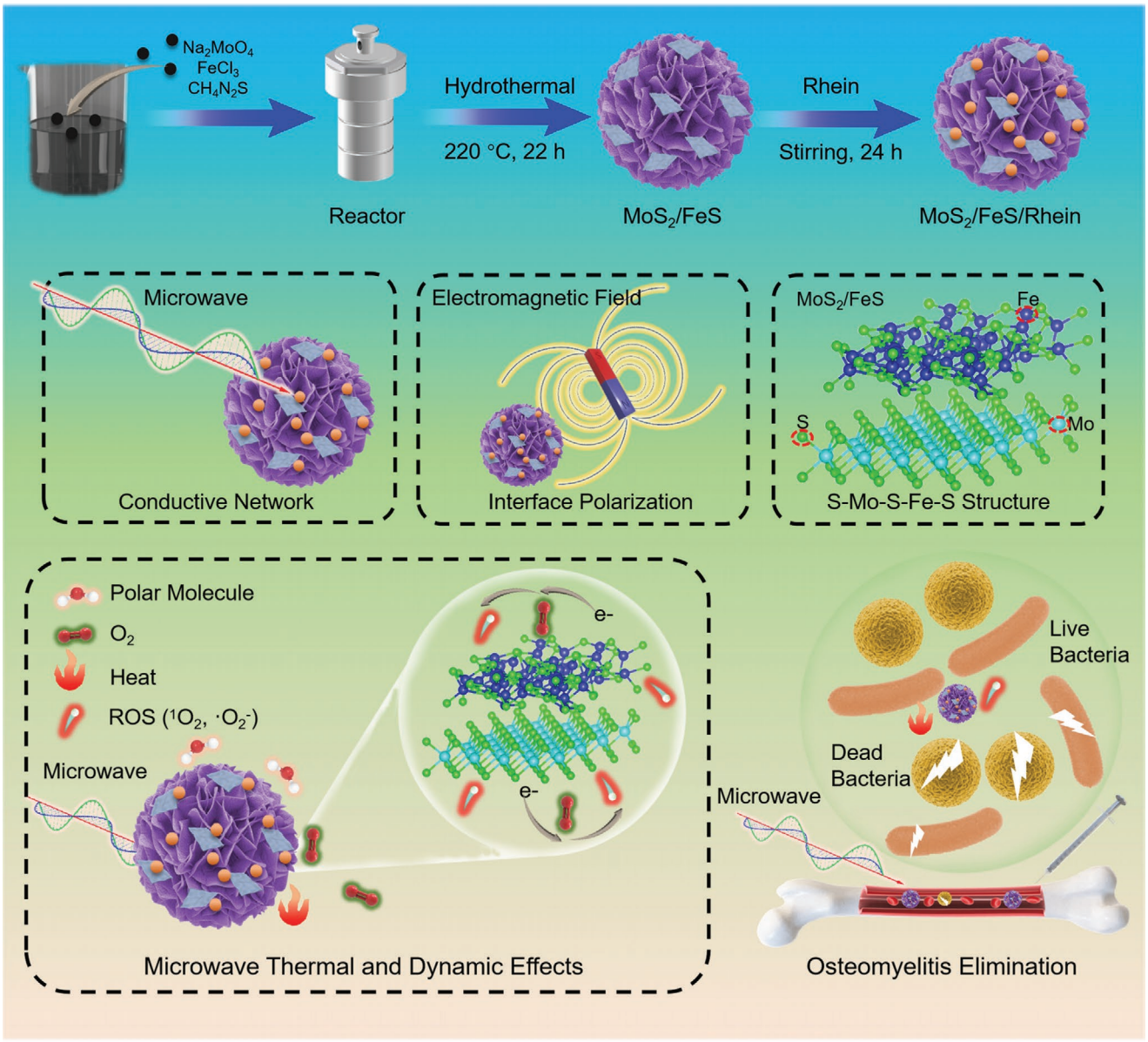

Figure 1. The MW-assisted therapeutic strategy for treating *S. aureus*-infected osteomyelitis by developing a MW-responsive nanocomposite of MoS_2/FeS modified by rhein. The prepared MoS_2/FeS/Rhe nanocomposite exhibited highly effective antibacterial efficacy and anti-inflammatory effect, which was attributed to the MW-triggered thermal effect and ROS as well as anti-inflammatory activity of Rhe. Under MW irradiation, dipoles or ions were aligned in an oscillating electric field, which caused dipolar polarization and ionic conduction, leading to molecular friction and dielectric loss to generate MW heat. In addition, the dipole orientation polarization caused by the interfacial polarization of MoS_2/FeS was the main factor for microwave catalysis.

and the potential of MoS_2/FeS was more negative than MoS_2, indicating that MoS_2 and FeS were successfully recombined. In addition, when MoS_2/FeS was recombined with negatively charged Rhe, the potential of MoS_2/FeS/Rhe was slightly positively charged, indicating that Rhe was loaded on the surface of MoS_2/FeS. The Fourier transform infrared (FTIR) spectroscopy of MoS_2/FeS/Rhe compared with MoS_2/FeS, the peaks at 1030 and 3430 cm^{-1} were attributed to the vibration of C—O and O—H in the Rhe, thus the obvious absorption peaks in the FTIR obtained from the MoS_2/FeS/Rhe confirmed that Rhe was successfully loaded onto MoS_2/FeS (Figure 2k). MoS_2/FeS/Rhe in water, saline, fetal bovine serum (FBS), and Dulbecco's modified eagle medium (DMEM) did not precipitate after setting 1 h, which proved that MoS_2/FeS/Rhe was relatively stable under complex physiological conditions (Figure S5, Supporting Information).

2.2. Microwave-Thermal and Microwave-Dynamic Effects of MoS_2/FeS/Rhe

A medical low power intensity of MW (2.45 GHz, 0.1 W cm^{-2}) was chosen to avoid the damage of healthy tissue caused by higher temperature. MW mainly transfers energy through

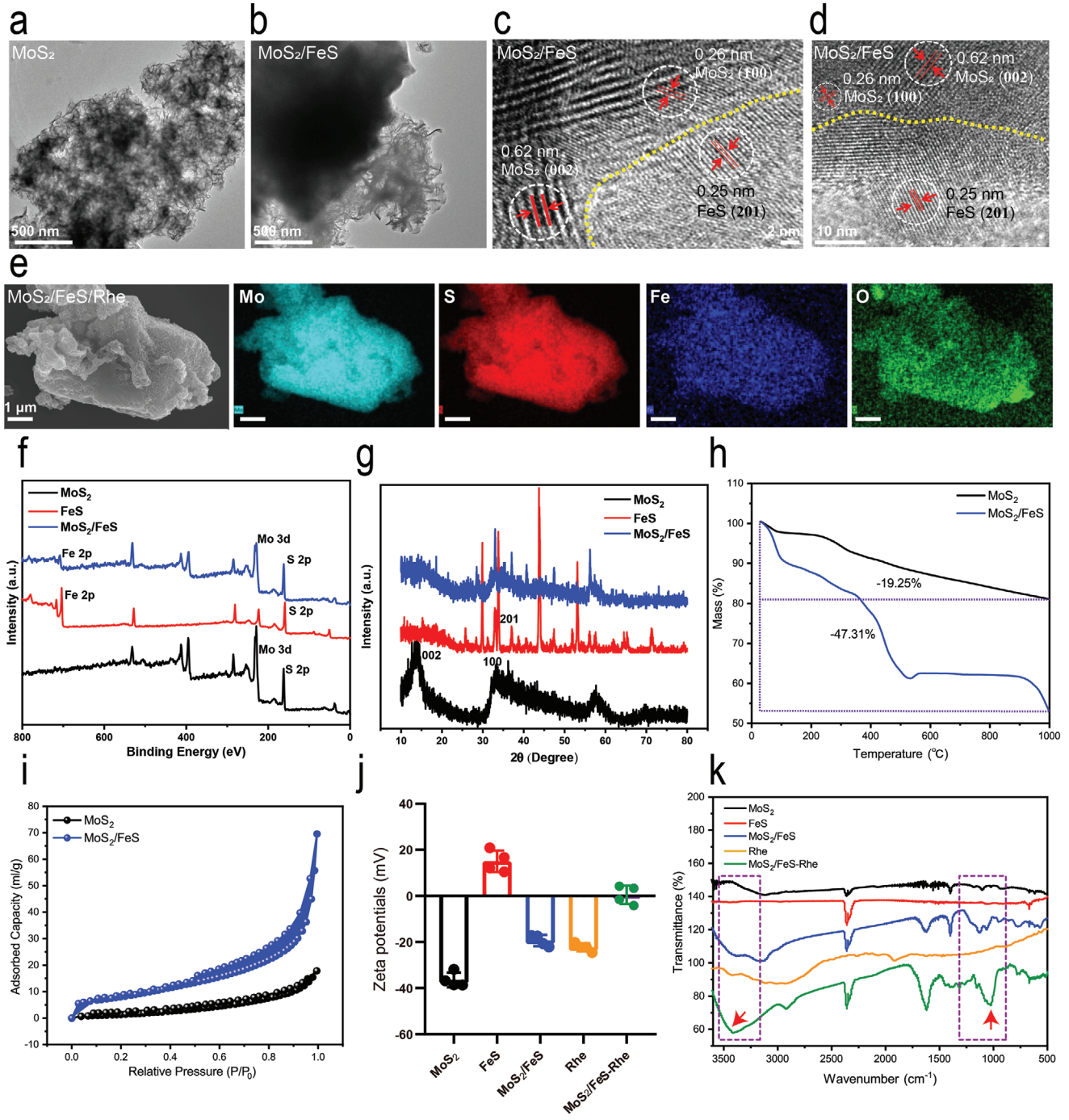

Figure 2. Preparation and characterization of MoS_2/FeS/Rhe. a) TEM image of MoS_2. b) TEM image of MoS_2/FeS. c) HRTEM image of MoS_2/FeS, yellow line represents an obvious interface. d) HRTEM image of MoS_2/FeS, yellow line represents an obvious interface. e) SEM image and elemental mapping of MoS_2/FeS/Rhe. f) XPS spectra of MoS_2, FeS, and MoS_2/FeS. g) XRD spectra of MoS_2, FeS, and MoS_2/FeS. h) TG curves of MoS_2 and MoS_2/FeS. i) Nitrogen adsorption–desorption curves of MoS_2 and MoS_2/FeS. j) Zeta potential of different samples. k) FTIR spectra of different samples.

electromagnetic fields. As shown in **Figure 3**a, under MW irradiation, the temperature of 1 mg mL^{-1} MoS_2/FeS solution increased to 62.6 °C only after 6 min. In contrast, the one of the saline was only raised to 55.3 °C under the same condition. The Rhe solution exhibited the similar temperature with that of the saline, suggesting that Rhe had no obvious MW thermal response. Under the same condition, the temperature of MoS_2/FeS/Rhe solution increased to 61.8 °C, indicating that the Rhe modification did not affect the MW thermal effect of MoS_2/FeS. The electron spin resonance (ESR) was employed to detect ROS production with 2,2,6,6-tetramethylpiperidine (TEMP) and 5,5-dimethyl-1-pyrroline-N-oxide (DMPO) as the capture agent for singlet oxygen ($^1O_2$) and superoxide anion ($\cdot O_2^-$), respectively.[28] It could be observed that MoS_2, FeS and

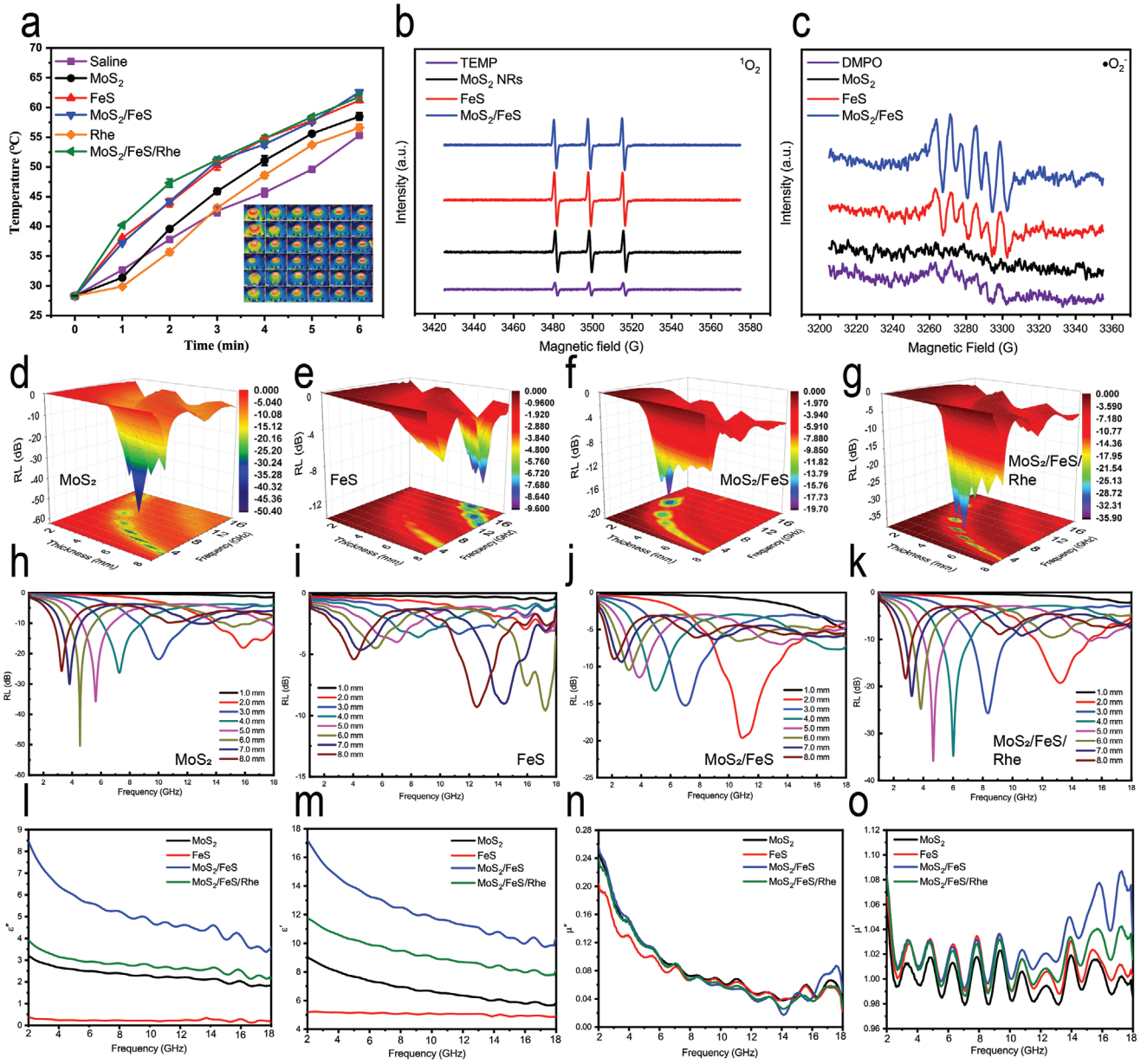

Figure 3. Microwave thermal response mechanism of MoS_2/FeS. a) Heating curves of different samples (1 mg mL^{-1}) under MW irradiation (2.45 GHz, 0.1 W cm^{-2}). Nested pictures were real-time infrared thermal imaging. b) ESR spectra of $^1O_2$ under MW radiation. c) ESR spectra of $\cdot O_2^-$ under MW radiation. 3D plots of frequency dependence: d) MoS_2; e) FeS; f) MoS_2/FeS; g) MoS_2/FeS/Rhe. Reflection loss (RL) curves: h) MoS_2; i) FeS; j) MoS_2/FeS; k) MoS_2/FeS/Rhe. l) Imaginary part of the permittivity in the range 2–18 GHz. m) Real part of the permittivity in the 2–18 GHz range. n) Imaginary part of permeability in the range 2–18 GHz. o) Real part of the permeability in the range 2–18 GHz.

MoS_2/FeS could all produce $^1O_2$ (Figure 3b), while FeS and MoS_2/FeS could produce $\cdot O_2^-$ under MW radiation (Figure 3c).

2.3. Microwave Thermal Response Mechanism of MoS_2/FeS/Rhe

To elucidate MW thermal mechanism of MoS_2/FeS, the reflection loss (RL) value was measured. According to our previous studies, a lower RL value means that more MW is absorbed, indicating an excellent MW thermal effect.[4,5] At 2.45 GHz, RL value of MoS_2 and FeS was –0.20 and –0.17 dB, respectively, indicating the lower MW absorption performance of the two materials (Figure 3d,e). In comparison, the RL value of MoS_2/FeS dropped to –8.29 dB at 2.45 GHz, and the frequency bandwidth shifted from the high frequency to the low frequency, indicating that the synthesized MoS_2/FeS had a high MW absorption performance (Figure 3f). After combining with Rhe, the RL value of MoS_2/FeS/Rhe was –11.75 dB at 2.45 GHz, indicating that the MW absorption performance of MoS_2/FeS/Rhe was enhanced after combination with Rhe (Figure 3g). RL curves demonstrated the same results, except for 3D plots of frequency dependence (Figure 3h–k). It has been reported

that the decay constant (α) is an important factor for materials to achieve high MW absorption performance.[5] As shown in Figure S6a, Supporting Information, the higher α value of MoS_2/FeS proved that the more incident MW was absorbed and converted into heat. The electromagnetic parameters with permittivity (ε) and permeability (μ) were further determined. Real part (ε', μ') of electromagnetic parameters represents absorption while Imaginary part (ε'', μ'') represents loss. The larger loss factor suggests the stronger coupling ability between the material and the MW. MoS_2/FeS exhibited a higher dielectric loss compared with MoS_2 and FeS at 2.45 GHz. Both real and imaginary permittivity values decreased with increasing frequency. Furthermore, MoS_2/FeS exhibited higher magnetic losses compared with MoS_2 and FeS at 2.45 GHz (Figure 3l–o). It could be found from the μ'' $(\mu')^{-2}$ f^{-1} curve that the value tended to be stable with the frequency change, indicating that the eddy current effect occurred in this process, indicating that the hysteresis loss was the main source of magnetic loss (Figure S6b, Supporting Information). The frequency dispersion characteristics dominated by the dielectric relaxation and the eddy current effect proved that the MW absorption capacity of MoS_2/FeS mainly came from the dielectric loss and magnetic loss, suggesting its better MW absorption performance with higher permittivity and permeability.

2.4. Microwave Dynamical Mechanism of MoS_2/FeS/Rhe

The density functional theory (DFT) calculations and finite element method (FEM) (COMSOL Multiphysics) were performed to explain the mechanism of MW dynamic effect. Regarding DFT calculations, compared with FeS (201) surface (−2.572 eV) and MoS_2 (002) surface (0.004 eV), the oxygen (O_2) adsorption energy of MoS_2/FeS surface was found to be −2.159 eV, indicating that MoS_2/FeS was easier to fix O_2 than MoS_2 (**Figure 4**a–c). According to FEM, the electromagnetic field enhancement parameters of MoS_2 and FeS were only 1.2 and 144.1, respectively. In contrast, the one of MoS_2/FeS interface reached up to 4699.5 (Figure 4d–f), which was attributed to that factor that the electromagnetic field enhancement induced the formation of electromagnetic hot spots at the MoS_2/FeS interface, which provided a large number of active sites for MW catalytic activity. The greater MW catalytic capacity of MoS_2/FeS resulted in the production of a mass of ROS. The detailed process of MW catalysis could be explained by the following two factors. First, MoS_2/FeS had a stronger O_2 fixation ability than MoS_2, which could provide more O_2 source to capture hotspots. Second, more electromagnetic hotspots could be generated at the interface of MoS_2/FeS compared with MoS_2 under MW irradiation due to interface polarization. Because of these induced electromagnetic hotspots, sodium species was field-ionized and subsequently reacted with oxygen to produce $^1O_2$ and $\cdot O_2^-$.

According to the photoluminescence (PL) spectra, the absorption peaks of MoS_2, FeS, and MoS_2/FeS in saline decreased after MW irradiation (Figure 4g–j), but no reduction in aqueous (Figure S7, Supporting Information). It was found that both MW and sodium species were favorable for electrons generation, but the MW energy alone was not sufficient to generate electrons in aqueous. According to previous study, in saline medium, potassium and sodium species can be ionized by strong electric field strength fields.[3] Therefore, it could be speculated that the sodium species in saline resonated with MW radiation to form plasmons and free electrons, which were further captured by surrounding oxygen species to generate free radicals. Next, the measured electrochemical impedance spectroscopy (EIS) disclosed that MoS_2/FeS had lower internal resistance, favoring the faster electron transfer (Figure 4k). The linear sweep voltammetry (LSV) and cyclic voltammetry (CV) curves shown in Figure 4l,m indicated that MoS_2/FeS had stronger current density and current transport capability. Furthermore, the MW current of MoS_2/FeS was much larger than the one of MoS_2 (Figure 4n), indicating that MoS_2/FeS had a stronger ability to generate electrons under MW irradiation. These results further verified the above conjecture.

2.5. In Vitro Antibacterial Activity of MoS_2/FeS/Rhe

To evaluate the antibacterial activity of the synthesized materials under MW irradiation, two representative bacteria, *Staphylococcus aureus* (*S. aureus*, Gram-positive bacteria) and *Escherichia coli* (*E. coli*, Gram-negative bacteria) were used for antibacterial tests. The antibacterial efficiency of MoS_2/FeS against *S. aureus* and *E. coli* almost reached 100% under MW irradiation (**Figure 5**a and Figure S8, Supporting Information). In contrast, under the same condition, both MoS_2 and FeS exhibited weak antibacterial activities. Under the same condition, Rhe had no obvious antibacterial activity while MoS_2/FeS/Rhe exhibited almost the same antibacterial efficacy as MoS_2/FeS, indicating that rhein had no antibacterial activity. As shown in Figure 5b, the group of MoS_2/FeS/Rhe exhibited the largest protein leakage under MW irradiation. The live/dead (green/red) bacterial staining (Figure 5c,d) showed the complete red fluorescence intensity in MoS_2/FeS/Rhe group compared with the control group under MW irradiation, suggesting the complete death of bacteria in MW-irradiated MoS_2/FeS/Rhe group, which was in good agreement with spread plate results. The bacterial morphologies in different groups after MW irradiation were observed by SEM. It could be found that the MoS_2/FeS/Rhe group had the most severe bacterial rupture (Figure 5e,f). The original SEM pictures were shown in the Figures S9 and S10, Supporting Information. In conclusion, MoS_2/FeS/Rhe could induce membrane rupture under MW irradiation by disrupting cell membrane damage and the followed efflux of bacterial inside substances, finally causing the bacterial death.

2.6. In Vitro Biotoxicity of MoS_2/FeS/Rhe

Blood safety was assessed by measuring hemolysis rate of MoS_2/FeS/Rhe at different concentrations. As shown in **Figure 6**a, no significant hemolysis (<5%) of red blood cells (RBCs) was observed, indicating that MoS_2/FeS/Rhe had good blood compatibility. In addition, SEM images of RBCs was shown in Figure S11, Supporting Information. We evaluated the cytotoxicity of different samples using mouse embryo osteoblast precursor cells (MC3T3-E1) and NIH-3T3 mouse embryonic fibroblast (NIH-3T3). Cytotoxicity of these

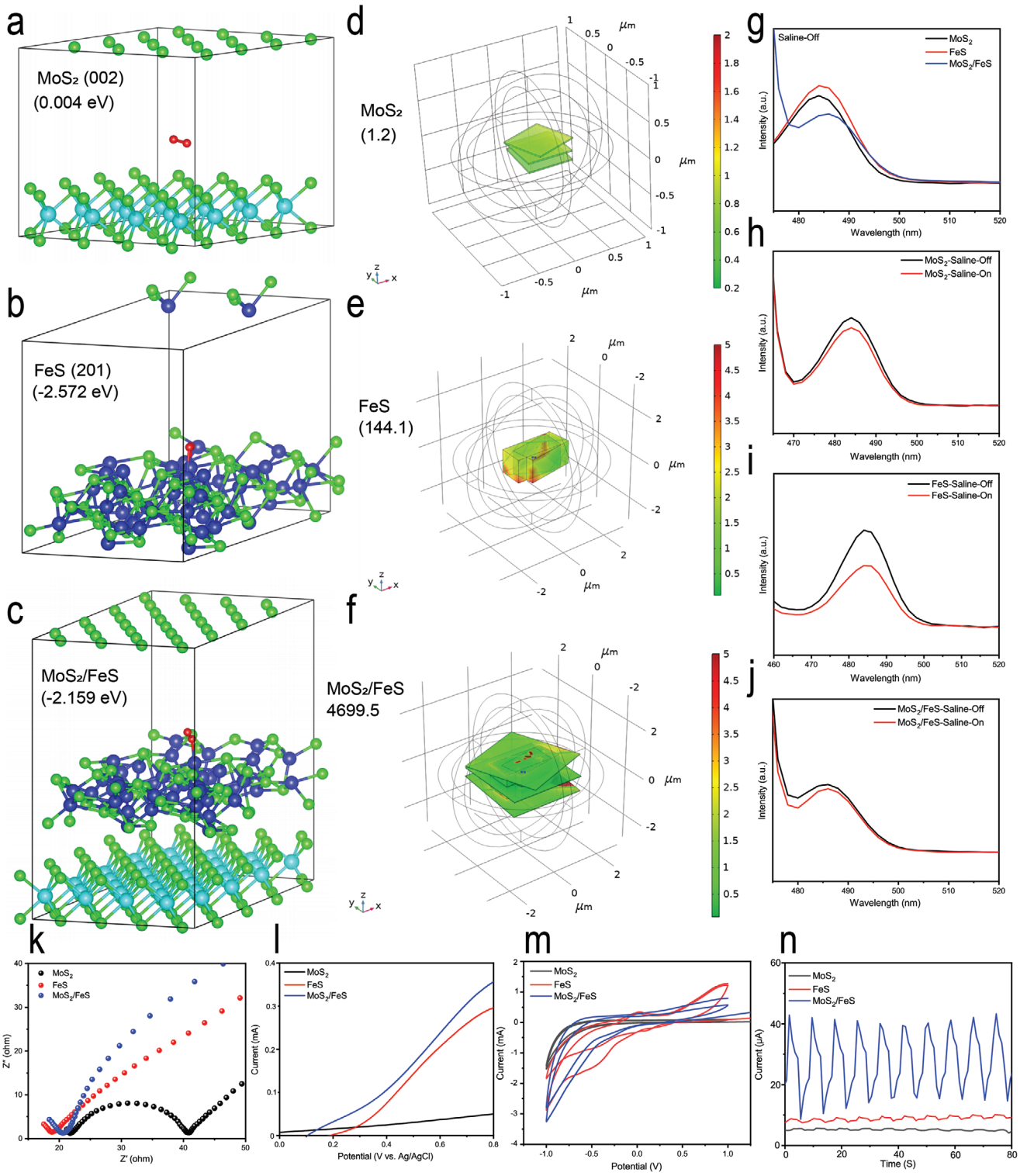

Figure 4. Microwave dynamic response mechanism of MoS_2/FeS. Geometric structures of a) MoS_2, b) FeS, and c) MoS_2/FeS. Cyan, green, blue and red represent Mo, S, Fe, and O atoms. FEM analysis of d) MoS_2, e) FeS, and f) MoS_2/FeS at 2.45 GHz. g) PL spectra of different samples (1 mg mL^{-1}). h) PL spectra of MoS_2 under different conditions (1 mg mL^{-1}). i) PL spectra of FeS under different conditions (1 mg mL^{-1}). j) PL spectra of MoS_2/FeS under different conditions (1 mg mL^{-1}). k) EIS curves of different samples. l) LSV curves of different samples. m) CV curves of different samples. n) Microwave currents of different samples under MW irradiation.

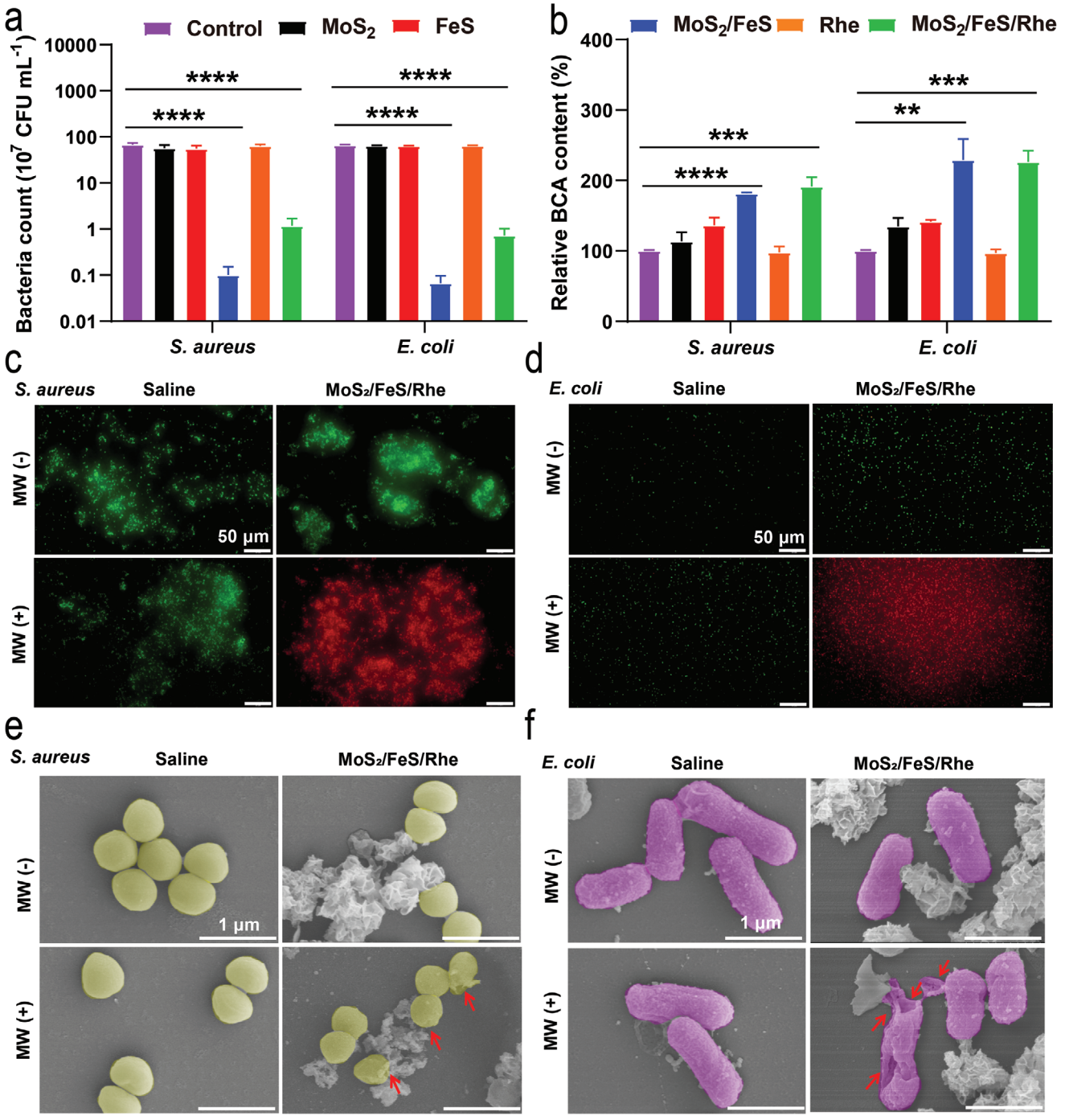

Figure 5. In vitro antimicrobial activity of MoS_2/FeS/Rhe. a) Antibacterial rates of different samples (1 mg mL^{-1}) against *S. aureus* and *E. coli* under MW irradiation ($n = 3$). b) Protein efflux in bacteria from different samples (1 mg mL^{-1}) under MW irradiation ($n = 3$). c) Live/dead staining of *S. aureus*, green/red fluorescence represents live/dead bacteria (Scale bar = 50 μm). d) Live/dead staining of *E. coli*, green/red fluorescence represents live/dead bacteria (Scale bar = 50 μm). e) SEM images of *S. aureus* (Scale bar = 1 μm), yellow represents *S. aureus* and red arrows represent bacterial rupture. f) SEM images of *E. coli* (Scale bar = 1 μm), purple represents *E. coli* and red arrows represent bacterial rupture. $^*P < 0.05$, $^{**}P < 0.01$, $^{***}P < 0.001$, $^{****}P < 0.0001$.

samples was assessed using the MTT assay. The viability of MC3T3-E1 cells and NIH-3T3 cells in the MoS_2/FeS/Rhe group was ≈90–100% compared with the control group after culturing for 1 and 3 days (Figure 6b,c). In addition, we used fluorescein isothiocyanate-labeled phalloidin (FITC, green)/4,6-diamino-2-phenyl indole (DAPI, blue) cell fluorescent staining to analyze cell morphology. MC3T3-E1 cells in MoS_2/FeS/Rhe was well distributed (Figure 6d). Previous study have shown that the loss of mitochondrial membrane potential (MMP) reduces cell viability, and the high MMP

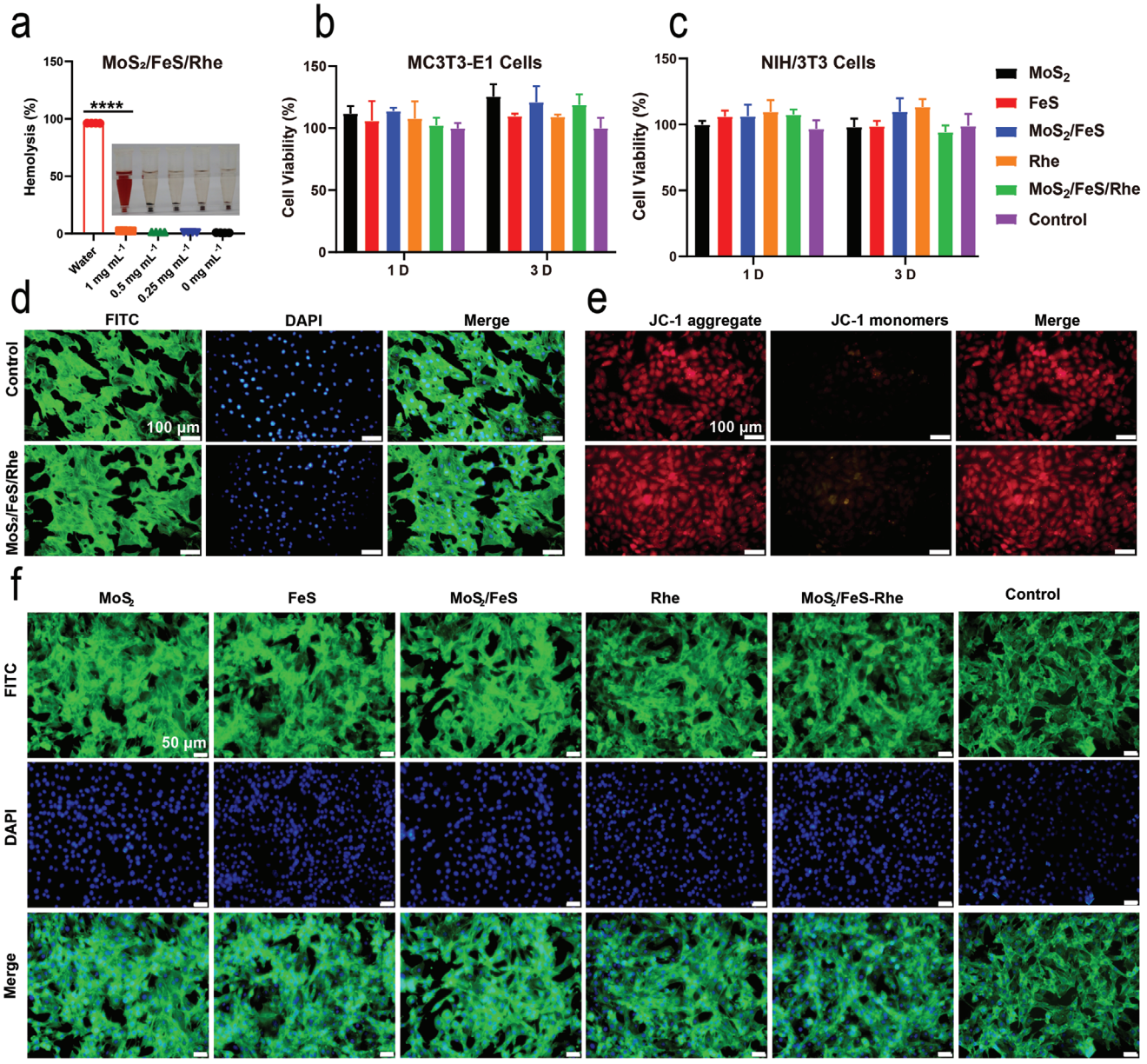

Figure 6. In vitro biotoxicity of MoS_2/FeS/Rhe. a) Hemolysis rates of MoS_2/FeS/Rhe at different concentrations (n = 4). b) MTT cell viability of MC3T3-E1 cells coculture with different samples (1 mg mL^{-1}) (n = 3). c) MTT cell viability of NIH-3T3 cells coculture with different samples (1 mg mL^{-1}) (n = 3). d) FITC/DAPI fluorescence images of MC3T3-E1 cells coculture with MoS_2/FeS/Rhe (1 mg mL^{-1}) for day 1 (Scale bar = 100 μm). e) JC-1 fluorescence images of MC3T3-E1 cells coculture with MoS_2/FeS/Rhe (1 mg mL^{-1}) for day 1 (Scale bar = 100 μm). f) FITC/DAPI fluorescence images of NIH-3T3 cells coculture with different samples (1 mg mL^{-1}) for day 1 (Scale bar = 50 μm). *P < 0.05, **P < 0.01, ***P < 0.001, ****P < 0.0001.

results in a significant increase in the ratio of red to green fluorescence (R/G).[29] As shown in Figure 6e, according to 5,5′,6,6′-Tetrachloro-1,1′,3,3′-tetraethyl-imidacarbocyanine (JC-1) cell fluorescent staining, compared with the control group, MC3T3-E1 cells showed no significant difference after coculture with MoS_2/FeS/Rhe for 1 day. Likewise, NIH-3T3 cells in MoS_2/FeS/Rhe group exhibited similar results for (Figure 6f). These results all indicated that the synthesized MoS_2/FeS/Rhe had excellent biocompatibility.

2.7. In Vivo Osteomyelitis Treatment with MoS_2/FeS/Rhe

As shown in Figure S12, Supporting Information, we established an osteomyelitis model on mouse tibia to study in vivo antibacterial and anti-inflammatory effects of MoS_2/FeS/Rhe. Mice were divided into three groups: the control group (*S. aureus*), MoS_2/FeS/Rhe (MoS_2/FeS/Rhe + *S. aureus*), MoS_2/FeS/Rhe + MW (MoS_2/FeS/Rhe + MW + *S. aureus*). Thermal images showed that the temperature could rise to 53.9 °C

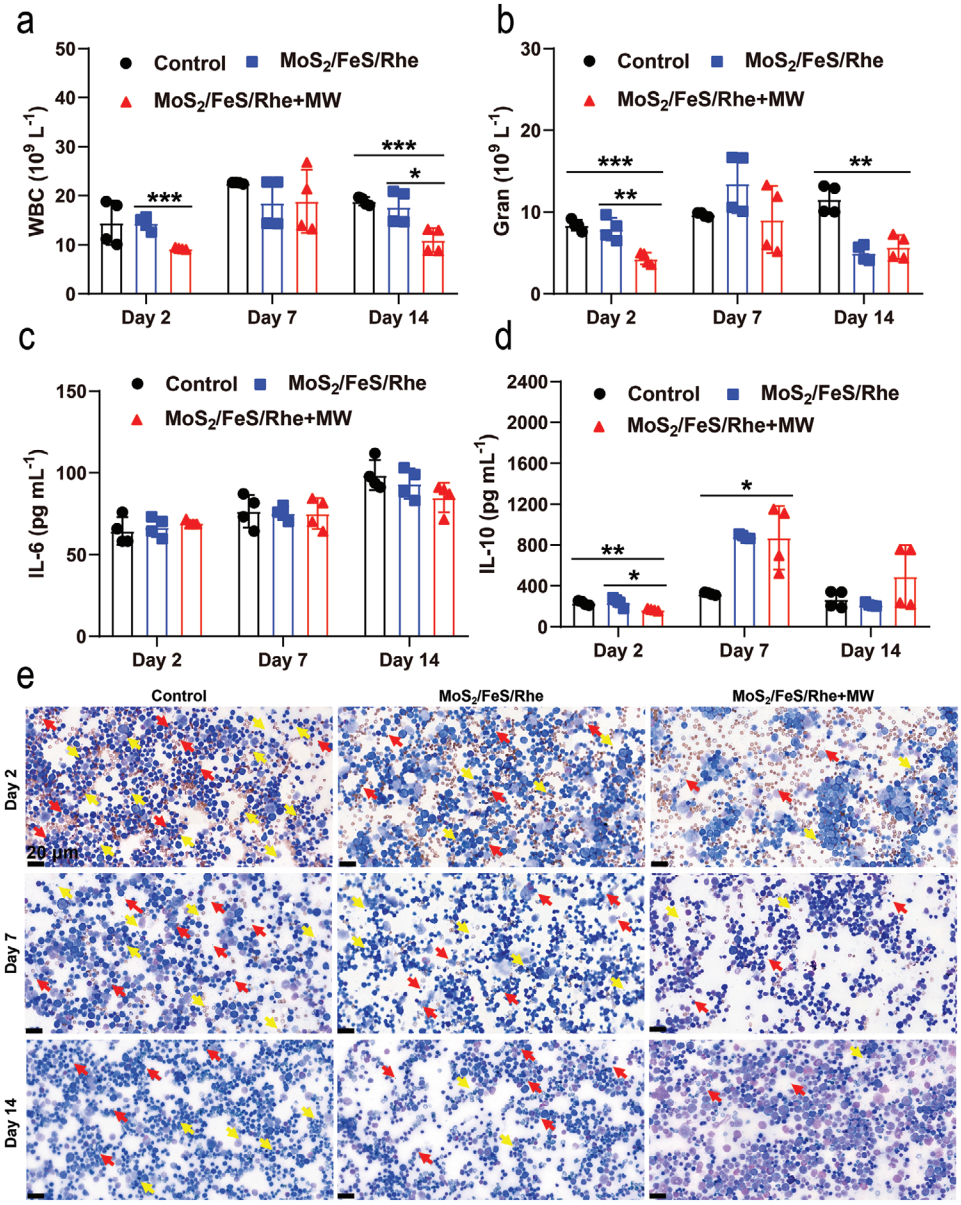

Figure 7. In vivo osteomyelitis treatment of MoS_2/FeS/Rhe. a) WBC, b) Gran, c) IL-6, and d) IL-10 after different time of treatment ($n = 4$). e) Wright-stained images of infected bone marrow tissue after treatment for different times (Scale bar = 20 μm), red arrows indicate bacteria and yellow arrows indicate lymphocytes. *$P < 0.05$, **$P < 0.01$, ***$P < 0.001$, ****$P < 0.0001$.

under MW irradiation, indicating that MoS_2/FeS/Rhe still had a good MW thermal effect in vivo (Figure S13, Supporting Information). The colony count assays were performed using bone marrow tissues, livers, and kidneys on day 2, and results showed that the MoS_2/FeS/Rhe + MW group consistently exhibited the greatest antibacterial efficacy against *S. aureus* in vivo (Figure S14, Supporting Information). The blood analysis obtained from the mice sacrificed at 2, 7, and 14 days was carried out using routine blood counts and blood biochemical analyses to assess the inflammatory response. It could be found that white blood cells (WBC) and neutrophils (Gran) in the MoS_2/FeS/Rhe + MW group were consistently significantly lower than the one in the control group (**Figure 7**a,b). In addition, the expression of proinflammatory factor interleukin 6 (IL-6) decreased and the expression of anti-inflammatory factor interleukin 10 (IL-10) increased with the prolongation of treatment time (Figure 7c,d). These results indicated that MoS_2/FeS/Rhe had a good antibacterial and anti-inflammatory effect in vivo due to the produced MW heat and ROS ($^1O_2$, $\cdot O_2^-$), as well as the anti-inflammatory effect of Rhe. In addition, Wright staining and hematoxylin–eosin (H&E) staining were used to further evaluate the rat tibia tissue infection. As shown in Figure 7e, the numbers of bacteria (indicated by red arrows) and lymphocytes (indicated by yellow arrows) in the MoS_2/FeS/Rhe + MW group decreased on day 14. However, distinct bacteria and lymphocytes were observed in the control group. According

to the H&E staining images, a large number of inflammatory cells (yellow arrows) and neutrophils (blue arrows) appeared in the control group. However, the inflammatory cells in the bone marrow tissue of the MoS_2/FeS/Rhe + MW group were significantly reduced (Figure S15, Supporting Information). After 14 days of treatment, the H&E staining images of mouse major organs (heart, liver, spleen, lung, and kidney) showed that MW treatment did not cause organ damage (Figure S16, Supporting Information). The above results indicated that MW-irradiated MoS_2/FeS/Rhe was a safe and effective strategy for treating bacteria-induced osteomyelitis in deep tissues.

3. Discussion

In this study, we reported a MW assisted bacteria-killing strategy for treating *S. aureus*-induced osteomyelitis by using MW-responsive MoS_2/FeS heterojunction with anti-inflammatory herb of Rhe thereby avoiding multiple surgical debridements and systemic injections of large amounts of antibiotics. Our data indicated that MW had deep penetration ability and negligible side effects, which could be a safe and effective therapeutic tool. MoS_2 can cause dipole polarization and ion conduction under MW radiation, resulting in molecular friction and dielectric loss to generate MW heat,[13,17–19] but its inherent weak conductivity and few polarization active sites limits its application in the field of microwave absorption.[20,21] MoS_2 combined with various components of dielectric or magnetic types for the construction of MoS_2-based absorbers such as MoS_2/rGO,[22] MoS_2@C,[23] and MoS_2/Fe_3O_4,[24] have been considered as typical strategies and have shown great potential for improving microwave absorption performance. Our data indicated that MoS_2/FeS could possess MW heat and generate ROS due to interfacial interactions benefiting from S-Mo-S-Fe-S structure, which may be promising high-performance MTT and MDT reagent.

Anti-inflammatory are also a major concern in the treatment of osteomyelitis, and natural herbal medicines such as rhein, berberine, curcumin, and puerarin, were promising for treating inflammation.[26,27] Our data indicated that Rhe widely distributed in the rhizomes of the olygonaceae plant Rheumpalmatum L., the roots of Polygonum multiflorum Thunb., and the pods of the legume Cassiaangustifolia Vahl., had anti-inflammatory effects. ROS can assist thermal effect to kill bacteria at a moderate temperature without scalding surrounding tissues.[14] ESR is employed to detect ROS production with TEMP and DMPO as the capture agent.[28] Our data indicated that MoS_2/FeS could produce ROS ($^1O_2$ and $\cdot O_2^-$) under MW radiation. A lower RL value means that more MW is absorbed, indicating an excellent MW thermal effect.[4,5] Our data indicated that the RL value of MoS_2/FeS/Rhe was −11.75 dB at 2.45 GHz, indicating that the MW absorption performance of MoS_2/FeS/Rhe was enhanced compared with individual components. MoS_2/FeS/Rhe could induce membrane rupture under MW irradiation by disrupting cell membrane damage and the followed efflux of bacterial inside substances, finally causing the bacterial (*S. aureus*, Gram-positive bacteria and *E. coli*, Gram-negative bacteria) death. The excellent biocompatibility of MoS_2/FeS/Rhe was demonstrated by blood safety, MTT assay of MC3T3-E1 and NIH-3T3 cells, FITC/DAPI cell fluorescent staining, and JC-1 cell fluorescent staining. In addition, MW-irradiated MoS_2/FeS/Rhe was a safe and effective strategy for treating *S. aureus*-induced osteomyelitis in deep tissues. This kind of MW responsive nanocomposite comprising inorganics and herbs can solve the challenge of how to effectively treat deep tissue infections.

4. Conclusions

In conclusion, we designed a MW-responsive system of anti-inflammatory nanocomposite, which exhibited highly efficient treatment of deep bacterial infection osteomyelitis. The powerful antibacterial effect of MoS_2/FeS/Rhe was attributed to anti-inflammatory effect of Rhe, MW-excited thermal and dynamic effects. The MW network vector analysis, density functional theory and finite element modeling disclosed that the strong MW absorption capacity of MoS_2/FeS mainly came from the dielectric loss of reflection loss while its enhanced MW catalysis was attributed to its stronger O_2 fixation ability than MoS_2 alone, which provided more O_2 source to capture electromagnetic hotspots. Additionally, more electromagnetic hotspots were generated at MoS_2/FeS interface than MoS_2 under MW irradiation due to interface polarization. Because of these induced electromagnetic hotspots, sodium species was field-ionized and subsequently reacted with oxygen to produce ROS ($^1O_2$ and $\cdot O_2^-$). Both in vitro and in vivo experiments showed that MoS_2/FeS/Rhe exhibited good biocompatibility and antibacterial ability. With these advantages, this work provided a safe, remote, noninvasive, and highly effective for deep bacterial infections.

5. Experimental Section

Materials: Rhein (Rhe) was purchased from Shanghai Yuanye Biotechnology Co., Ltd. (Shanghai, China). Sodium chloride (NaCl), ferric chloride ($FeCl_3{\cdot}6H_2O$), sodium sulfate (Na_2SO4), sodium molybdate ($Na_2MoO_4{\cdot}2H_2O$), thiourea (CH_4N_2S), and dimethyl sulfoxide were purchased from Sinopharm Chemical Reagent Co., Ltd. Company (Shanghai, China). Live/dead bacterial viability kits of SYTO 9 and propidium iodide (PI) stains were purchased from Thermo Fisher Scientific (Shanghai, China). Trypsin, penicillin–streptomycin, FITC-labeled phalloidin, and DAPI were purchased from Yeasen (Shanghai, China). TEMP was purchased from Aladdin Biochemical Technology Co., Ltd. (Shanghai, China). 3-[4,5-Dimethylthiazol-2-yl]-2,5-diphenyltetrazolium bromide (MTT) was purchased from Sigma Chemical Co., Ltd. DMEM and FBS were purchased from Gibco (Shanghai, China). DMPO was purchased from Nippon Chemical Co., Ltd. BCA protein detection kit was purchased from Solarbio (Beijing, China). Other reagents and solvents were of analytical grade and were used without further purification.

Synthesis of MoS_2, FeS, MoS_2/FeS, and MoS_2/FeS/Rhe: MoS_2 was prepared according to previously reported literature.[13] Briefly, 0.76 g $Na_2MoO_4{\cdot}2H_2O$ and 1.2 g CH_4N_2S were dispersed in 25 mL deionized water and sonicated to form a homogeneous solution. Next, 12 mL HCl (1 mol L^{-1}) was added to the solution for uniform dispersion, and the resulting solution was transferred to a 45 mL volume autoclave and heated at 220 °C for 22 h. After hydrothermal reaction was completed, the obtained MoS_2 was centrifuged and washed with water, and then freeze-dried. The synthesis method of FeS was similar to MoS_2, with the main difference being that $Na_2MoO_4{\cdot}2H_2O$ was replaced by $FeCl_3{\cdot}6H_2O$. The synthesis method of MoS_2/FeS was similar to MoS_2, mainly adding

0.6 g $FeCl_3{\cdot}6H_2O$ in the synthesis step of MoS_2. MoS_2/FeS and Rhe (weight ratio of 50:1) were mixed and dispersed in deionized water, and after stirring for 24 h. The obtained precipitate was centrifuged and washed with water, and then lyophilized to obtain MoS_2/FeS/Rhe.

Characterization of MoS_2/FeS/Rhe: The morphologies were characterized by SEM (UK ZEISS, Sigma300/500) and TEM (Japan JEOL, JEM-2100F). FTIR spectra were collected on a Fourier transform infrared spectrometer (IS10, Thermo Fisher Scientific, USA). Zeta potential was measured on a particle size and potentiometer (Zeta-sizer Nano ZS90, Malvern, UK). XPS spectra were collected on an X-ray photoelectron spectrometer (Axis Supra, Kratos HT, Japan). UV–vis diffuse reflectance spectra were collected on an ultra violet and visible light (UV–vis) absorption spectrometer (UV-2600, Shimadzu, Japan). XRD spectra were obtained on an X-ray diffractometer (Bruker, D8 ADVANCE, Germany). Raman scattering experiments were performed on a Raman microscope (DXR, Thermo Fisher Scientific, USA). Thermal absorption curves were collected on a thermogravimetric analyzer (NETZSCH, STA449C, Germany).

Measuring Microwave Heat: Microwave heating profiles were measured according to previously reported methods.[4] Briefly, 2 mL sample solutions (saline, MoS_2, FeS, MoS_2/FeS, Rhe, and MoS_2/FeS/Rhe of 1 mg mL^{-1}) were placed in a small dish (35 mm × 12 mm), which was placed on the microwave physiotherapy probe. The temperature changes of different samples under MW (0.1 W cm^{-2}) irradiation were recorded using a thermal imager (875i, Testo, GER).

ESR Test: 1 mL the sample solution was placed in a small dish (35 mm × 12 mm), which was placed on the microwave physiotherapy probe. Then an appropriate amount of capture agent TEMP or DMPO was added, and the solution was taken by capillary to test ESR spectra.

Microwave Network Vector Analysis: The electromagnetic parameters of the different samples were recorded using an Agilent E5071C network analyzer.[3–5] The reflection loss value (RL) and attenuation constant (α) were calculated as follows

$$RL = 20\left|\frac{Z_{in}-1}{Z_{in}+1}\right| \tag{1}$$

$$Z_{in} = \sqrt{|\mu_r/\varepsilon_r|}\tanh\left[j\left(\frac{2\pi df}{c}\right)\sqrt{\mu_r\varepsilon_r}\right] \tag{2}$$

$$\alpha = \frac{\sqrt{2}\pi f}{c}\sqrt{\left(\mu''\varepsilon'' - \mu'\varepsilon'\right) + \sqrt{\left(\mu''\varepsilon'' - \mu'\varepsilon'\right)^2 + \left(\mu'\varepsilon'' + \mu''\varepsilon'\right)^2}} \tag{3}$$

μ' and μ'' represent real and imaginary parts of the permeability. Z_{in} represents normalized input impedance. f represents frequency. d represents thickness of the monolayer absorber. ε' and ε'' represent real and imaginary parts of the permittivity. μ_r and ε_r represent relative permeability and permittivity, respectively. c represents speed of light.

DFT Calculations: All DFT calculations were performed using the VASP program.[3] The DFT functional was utilized at the Perdew–Burke–Ernzerhof level. A 2 × 2 × 1 gamma grid of k-points was used for the Brillounin zone integration. A Gaussian smearing of 0.2 eV was applied during the geometry optimization. The convergence criteria for the iteration in self-consistent field was set at 10–5 eV, and the residual force for optimizing atom positions was less than 0.02 eV $Å^{-1}$.

FEM Analysis: Finite element simulations were performed using the COMSOL Multiphysics 5.6 software.[3] In the simulations, the permittivity and permeability were measured experimentally. The permittivity of MoS_2 was 5.0863–1.1493$^*i$, and the magnetic permeability was 1.0000–0.2192$^*i$. The permittivity of FeS was 5.2289–0.3048$^*i$, and the magnetic permeability was 1.0149–0.1893$^*i$. The permittivity of MoS_2/FeS was 16.4510–7.7807$^*i$, and the magnetic permeability was 1.0235–0.2327$^*i$. In these calculations, the magnitude of the excited electric field was kept constant at 1 V m^{-1}.

PL Spectroscopy Test: 4 mg mL^{-1} MoS_2, FeS and MoS_2/FeS solutions were prepared with water and NaCl solution, and the changes of PL spectra were tested under microwave irradiation in situ. The excitation wavelength of MoS_2, FeS, and MoS_2/FeS was 430 nm.

Electrochemical Test: 4 mg mL^{-1} MoS_2, FeS, and MoS_2/FeS aqueous solutions were prepared and dropped evenly on the conductive glass (1 × 1 cm). During the process, air bubbles should be avoided, and they were naturally sealed for testing. Before testing the samples, the electrodes were rinsed with deionized water. After carefully checking that the electrodes were connected correctly (green of the working electrode, red of the platinum electrode, and white of the reference electrode), EIS curves, LSV curves, CV curves and microwave current were obtain by electrochemical test.

In Vitro Antibacterial Activity: To assess effect of different samples on *S. aureus* and *E. coli*, standard plate counts were used to assess bacterial concentrations. Briefly, 2 mL solutions of different sample were placed on small dishes (35 mm × 12 mm) and then irradiated under MW for 20 min (0.1 W cm^{-2}). Finally, 20 µL bacterial suspension was diluted 100 times and then spread on a standard plate, then photographed and counted after culturing at 37 °C for 24 h. To visualize distribution of live and dead bacteria, microwave-treated bacteria were stained by SYTO 9 and PI stains. The excitation/emission maxima for these dyes were about 480/500 nm for SYTO 9 stain (Component A) and 490/635 nm for propidium iodide (Component B). Equal volumes of Component A and Component B were combined in a microfuge tube, and mixed thoroughly. 3 µL of the dye mixture were added for each mL of the bacterial suspension. The dye mixture and the bacterial suspension were mixed thoroughly and incubated at room temperature in the dark for 15 min. 5 µL of the stained bacterial suspension were trapped between a slide and an 18 mm square coverslip, and observed in a fluorescence microscope (OLYMPUS, IX73). To observe morphology of bacteria after microwave treatment, SEM images acquisition was performed.

In Vitro Cytotoxicity: Mouse embryo osteoblast precursor cells (MC3T3-E1) and NIH-3T3 mouse embryonic fibroblast (NIH-3T3) were cultured in DMEM. The cytotoxicity of MoS_2, FeS, MoS_2/FeS, Rhe, and MoS_2/FeS/Rhe was determined by MTT.[5] The absorbance of the supernatant at 490 nm was measured on a microplate reader (Molecular Devices, SpectraMax M5). To further confirm MTT results, fluorescein isothiocyanate-labeled phalloidin (FITC)/4′,6-diamidino-2-phenylindole (DAPI) staining and 5,5′,6,6′-Tetrachloro-1,1′,3,3′-tetraethylimidacarbocyanine (JC-1) staining were carried out and imaged using an inverted fluorescence microscope. Cell viability was calculated by the following equation

$$\text{Cellviability} = \left(OD_{490nm/sample}/OD_{490nm/control}\right)\times 100\% \tag{4}$$

In Vitro Hemolysis Assay: Hemolysis assays were performed as previously reported.[29] Briefly, 0.15 mL red blood cells were combined with 0.15 mL various concentrations of MoS_2/FeS/Rhe solutions, water or saline. After 12 h of incubation at 37 °C, the mixture was centrifuged and the supernatant was collected, then the absorbance was measured at 542 nm using a microplate reader. The hemolysis rate was calculated using the following formula

$$\text{Hemolysis rate}\,(\%) = \left(I/I_0\right)\times 100\% \tag{5}$$

I refers to the optical density (OD) of erythrocytes with different concentrations of MoS_2/FeS/Rhe, and I_0 refers to OD of complete hemolysis in distilled water.

In Vivo Mouse Osteomyelitis Model: Male mice of 300–400 g were prepared for animal experiments. Mice were divided into three groups: control (*S. aureus*), MoS_2/FeS/Rhe (MoS_2/FeS/Rhe + *S. aureus*), and MoS_2/FeS/Rhe + MW (MoS_2/FeS/Rhe + MW + *S. aureus*). After the mice were anesthetized with isoflurane, 0.7 mm diameter holes were drilled in the mice tibia by electric drill. Bloods in the bone marrow cavity was drawn with a 1 mL syringe, and bacterial solution (2×10^8 CFU mL^{-1} *S. aureus*) and 50 µL saline or MoS_2/FeS/Rhe (1 mg mL^{-1}) were injected into the well. Afterward, the hole was sealed with bone wax, and the wound was carefully sutured. Finally, the surgical site was irradiated by the MW physiotherapy device for 20 min. Thermographic pictures were

recorded before and after irradiation by using a thermal imager (FLIR, E50). On days 2, 7, and 14, bloods were collected for routine blood tests and blood biochemical assays, and bone marrows were collected for H&E staining and Wright staining. After 14 days, major organs (heart, liver, spleen, lung, and kidney) were collected for H&E staining. The animal test was carried out following the guidance of the Guide for the Care and Use of Laboratory Animals of the National Institutes of Health. The Animal Ethical and Welfare Committee of the Institute of Radiation Medicine, Chinese Academy of Medical Sciences approved the ethical part of the experiment.

Statistical Analysis: All the experimental data did not involve preprocessing of data (such as transformation, normalization, and evaluation of outliers). All the experimental data were analyzed using mean ± standard deviation (SD) with $n \geq 3$. The statistical analyses were performed using the GraphPad Prism software, with one-way analysis of variance followed by the Tukey multiple-comparisons test for multiple comparisons and a two-sample Student *t*-test for comparison of two groups. In addition, *p* values were considered statistically significant. $^{*}P < 0.05$, $^{**}P < 0.01$, $^{***}P < 0.001$, $^{****}P < 0.0001$.

Supporting Information

Supporting Information is available from the Wiley Online Library or from the author.

Acknowledgements

This work is jointly supported by the China National Funds for Distinguished Young Scientists (No.51925104), the National Natural Science Foundation of China (Nos. 51871162, and 52173251), and NSFC-Guangdong Province Joint Program (Key program no. U21A2084).

Conflict of Interest

The authors declare no conflict of interest.

Data Availability Statement

The data that support the findings of this study are available from the corresponding author upon reasonable request.

Keywords

antibacterial, microwave therapy, molybdenum disulfide, osteomyelitis, rhein

Received: April 20, 2022
Revised: May 13, 2022
Published online: June 2, 2022

[1] a) D. P. Lew, F. A. Waldvogel, *Lancet* **2004**, *364*, 369; b) C. Y. Huang, R. W. Hsieh, H. T. Yen, T. C. Hsu, C. Y. Chen, Y. C. Chen, C. C. Lee, *Int. J. Antimicrob. Ag* **2019**, *53*, 246; c) Y. Li, L. N. Liu, P. Wan, Z. J. Zhai, Z. Y. Mao, Z. X. Ouyang, D. G. Yu, Q. Sun, L. L. Tan, L. Ren, Z. A. Zhu, Y. Q. Hao, X. H. Qu, K. Yang, K. R. Dai, *Biomaterials* **2016**, *106*, 250; d) E. A. Masters, B. F. Ricciardi, K. L. D. Bentley, T. F. Moriarty, E. M. Schwarz, G. Muthukrishnan, *Nat. Rev. Microbiol.* **2022**, *376*, 1; e) N. Kavanagh, E. J. Ryan, A. Widaa, G. Sexton, J. Fennell, S. O'Rourke, K. C. Cahill, C. J. Kearney, F. J. O'Brien, S. W. Kerrigan, *Clin. Microbiol. Rev.* **2018**, *31*, e00084-17.

[2] a) N. Jiang, H. T. Wu, Q. R. Lin, Y. J. Hu, B. Yu, *J. Surg. Res.* **2020**, *247*, 356; b) Y. Yu, L. Tan, Z. Y. Li, X. M. Liu, Y. F. Zheng, X. B. Feng, Y. Q. Liang, Z. D. Cui, S. L. Zhu, S. L. Wu, *ACS Nano* **2021**, *15*, 10628; c) X. B. Feng, J. Lei, L. Ma, Q. L. Ouyang, Y. X. Zeng, H. Liang, C. C. Lei, G. C. Li, L. Tan, X. M. Liu, C. Yang, *Small* **2021**, *18*, 2105775; d) P. P. Sedghizadeh, S. T. Sun, A. F. Junka, E. Richard, K. Sadrerafi, S. Mahabady, N. Bakhshalian, N. Tjokro, M. Bartoszewicz, M. Oleksy, P. Szymczyk, M. W. Lundy, J. D. Neighbors, R. G. G. Russell, C. E. McKenna, F. H. Ebetino, *J. Med. Chem.* **2017**, *60*, 2326; e) S. W. Jung, S. H. Oh, I. S. Lee, J. H. Byun, J. H. Lee, *Tissue Eng. Regen. Med.* **2019**, *16*, 479.

[3] J. N. Fu, Y. Li, Y. Zhang, Y. Q. Liang, Y. F. Zheng, Z. Y. Li, S. L. Zhu, C. Y. Li, Z. D. Cui, S. L. Wu, *Adv. Mater.* **2021**, *33*, 2102926.

[4] S. B. Wei, Y. Q. Qiao, Z. C. Wu, X. M. Liu, Y. Li, Z. D. Cui, C. Y. Li, Y. F. Zheng, Y. Q. Liang, Z. Y. Li, S. L. Zhu, H. R. Wang, X. B. Wang, R. C. Che, S. L. Wu, *Nano Today* **2021**, *37*, 101090.

[5] Y. Q. Qiao, X. M. Liu, B. Li, Y. Han, Y. F. Zheng, K. W. K. Yeung, C. Y. Li, Z. D. Cui, Y. Q. Liang, Z. Y. Li, S. L. Zhu, X. B. Wang, S. L. Wu, *Nat. Commun.* **2020**, *11*, 4446.

[6] a) M. Brummerstedt, M. Bangstrup, T. S. Barfod, *Spinal Cord Ser. Cases* **2018**, *4*, 59; b) H. Shoji, T. Urakawa, K. Watanabe, T. Hirano, K. Katsumi, M. Ohashi, T. Sato, A. Yamazaki, Y. Yajiri, R. Kikuchi, N. Hosaka, K. Sawakami, K. Miura, I. Nakamura, R. Fujikawa, M. Wakasugi, N. Endo, *J. Orthop. Sci.* **2016**, *21*, 282.

[7] a) J. E. Cassat, N. D. Hammer, J. P. Campbell, M. A. Benson, D. S. Perrien, L. N. Mrak, M. S. Smeltzer, V. J. Torres, E. P. Skaar, *Cell Host Microbe* **2013**, *13*, 759; b) K. L. Urish, J. E. Cassat, *Infect. Immun.* **2020**, *88*, e00932-19; c) Z. B. Zhou, C. H. Pan, Y. Lu, Y. S. Gao, W. Liu, P. P. Yin, X. W. Yu, *Front. Cell. Infect. Microbiol.* **2017**, *7*, 379; d) A. Widaa, T. Claro, T. J. Foster, F. J. O'Brien, S. W. Kerrigan, *PLoS One* **2012**, *7*, e40586; e) C. E. Butrico, J. E. Cassat, *Toxins (Basel)* **2020**, *12*, 516.

[8] a) S. Hussain, J. Joo, J. Kang, B. Kim, G. B. Braun, Z. G. She, D. Kim, A. P. Mann, T. Molder, T. Teesalu, S. Carnazza, S. Guglielmino, M. J. Sailor, E. Ruoslahti, *Nat. Biomed. Eng.* **2018**, *2*, 95; b) X. L. Lu, R. H. Chen, J. Lv, W. C. Xu, H. J. Chen, Z. B. Ma, S. S. Huang, S. Li, H. Liu, J. Hu, L. M. Nie, *Acta. Biomater.* **2019**, *99*, 363; c) M. Diefenbeck, C. Schrader, F. Gras, T. Muckley, J. Schmidt, S. Zankovych, J. Bossert, K. D. Jandt, A. Volpel, B. W. Sigusch, H. Schubert, S. Bischoff, W. Pfister, B. Edel, M. Faucon, U. Finger, *Biomaterials* **2016**, *101*, 156; d) N. W. Cortes-Penfield, P. A. Kulkarni, *Open Forum Infect. Dis.* **2019**, *66*, ofz181; e) A. Ghimire, J. D. Skelly, J. Song, *ACS Central Sci.* **2019**, *5*, 1929.

[9] a) B. D. Gimza, J. E. Cassat, *Front. Immunol.* **2021**, *12*, 638085; b) R. A. Fisher, B. Gollan, S. Helaine, *Nat. Rev. Microbiol.* **2017**, *15*, 453; c) J. M. Stokes, K. Yang, K. Swanson, W. G. Jin, A. Cubillos-Ruiz, N. M. Donghia, C. R. MacNair, S. French, L. A. Carfrae, Z. Bloom-Ackerman, V. M. Tran, A. Chiappino-Pepe, A. H. Badran, I. W. Andrews, E. J. Chory, G. M. Church, E. D. Brown, T. S. Jaakkola, R. Barzilay, J. J. Collins, *Cell* **2020**, *180*, 688; d) H. Kyriacou, A. Kamaraj, W. S. Khan, *Appl. Sci. Basel* **2020**, *10*, 7554.

[10] a) J. M. Sadowska, K. J. Genoud, D. J. Kelly, F. J. O'Brien, *Mater. Today* **2021**, *46*, 136; b) J. Li, X. M. Liu, L. Tan, Z. D. Cui, X. J. Yang, Y. Q. Liang, Z. Y. Li, S. L. Zhu, Y. F. Zheng, K. W. K. Yeung, X. B. Wang, S. L. Wu, *Nat. Commun.* **2019**, *10*, 4490; c) Z. Yuan, B. L. Tao, Y. He, C. Y. Mu, G. H. Liu, J. X. Zhang, Q. Liao, P. Liu, K. Y. Cai, *Biomaterials* **2019**, *223*, 119479; d) W. Guan, L. Tan, X. M. Liu, Z. D. Cui, Y. F. Zheng, K. W. K. Yeung, D. Zheng, Y. Q. Liang, Z. Y. Li, S. L. Zhu, X. B. Wang, S. L. Wu, *Adv. Mater.* **2021**, *33*, 2006047; e) D. L. Han, P. L. Yu, X. M. Liu, Y. D. Xu, S. L. Wu, *Rare Met.* **2022**, *41*, 663; f) R. Lv, Y. Q. Liang, Z. Y. Li, S. L. Zhu, Z. D. Cui, S. L. Wu, *Rare Met.* **2022**, *41*, 639.

[11] a) L. G. Jin, H. X. Cheng, X. P. Xie, X. Y. Chen, G. Q. Tian, Z. L. Zhu, S. H. Wang, H. B. Xin, X. L. Wang, *Adv. Healthcare Mater.* **2021**, *10*, 2001966; b) B. L. Liu, Y. T. Su, S. S. Wu, J. Shen, *New J. Chem.* **2021**, *45*, 18124; c) C. Y. Mao, Y. M. Xiang, X. M. Liu, Y. F. Zheng, K. W. K. Yeung, Z. D. Cui, X. J. Yang, Z. Y. Li, Y. Q. Liang, S. L. Zhu, S. L. Wu, *ACS Appl. Mater. Interfaces* **2019**, *11*, 17902.

[12] a) T. Y. Tang, X. M. Xu, Z. W. Wang, J. J. Tian, Y. Yang, C. Z. Ou, H. H. Bao, T. L. Liu, *Chem. Commun.* **2019**, *55*, 13148; b) Z. Chen, M. Niu, G. Chen, Q. Wu, L. Tan, C. Fu, X. Ren, H. Zhong, K. Xu, X. Meng, *ACS Nano* **2018**, *12*, 12721; c) C. Fu, H. Zhou, L. Tan, Z. Huang, Q. Wu, X. Ren, J. Ren, X. Meng, *ACS Nano* **2018**, *12*, 2201.

[13] S. P. Wang, L. F. Tan, P. Liang, T. L. Liu, J. Z. Wang, C. H. Fu, J. Yu, J. P. Dou, L. Hong, X. W. Meng, *J. Mater. Chem. B* **2016**, *4*, 2133.

[14] a) X. M. Xu, X. M. Liu, L. Tan, Z. D. Cui, X. J. Yang, S. L. Zhu, Z. Y. Li, X. B. Yuan, Y. F. Zheng, K. W. K. Yeung, P. K. Chu, S. L. Wu, *Acta. Biomater.* **2018**, *77*, 352; b) M. Li, L. Q. Li, K. Su, X. M. Liu, T. J. Zhang, Y. Q. Liang, D. D. Jing, X. J. Yang, D. Zheng, Z. D. Cui, Z. Y. Li, S. L. Zhu, K. W. K. Yeung, Y. F. Zheng, X. B. Wang, S. L. Wu, *Adv. Sci.* **2019**, *6*, 1900599.

[15] a) L. Liang, Q. Li, X. Yan, Y. Feng, Y. Wang, H. B. Zhang, X. Zhou, C. Liu, C. Shen, X. Xie, *ACS Nano* **2021**, *15*, 6622; b) C. Y. Wen, X. Li, R. X. Zhang, C. Y. Xu, W. B. You, Z. W. Liu, B. A. Zhao, R. C. Che, *ACS Nano* **2021**, *16*, 1150; c) L. Wang, X. F. Yu, X. Li, J. Zhang, M. Wang, R. C. Che, *Carbon* **2019**, *155*, 298; d) Y. Li, X. F. Liu, X. Y. Nie, W. W. Yang, Y. D. Wang, R. H. Yu, J. L. Shui, *Adv. Funct. Mater.* **2019**, *29*, 1807624; e) Z. C. Wu, K. Pei, L. S. Xing, X. F. Yu, W. B. You, R. C. Che, *Adv. Funct. Mater.* **2019**, *29*, 1901448.

[16] a) A. K. Geim, I. V. Grigorieva, *Nature* **2013**, *499*, 419; b) J. N. Coleman, M. Lotya, A. O'Neill, S. D. Bergin, P. J. King, U. Khan, K. Young, A. Gaucher, S. De, R. J. Smith, I. V. Shvets, S. K. Arora, G. Stanton, H. Y. Kim, K. Lee, G. T. Kim, G. S. Duesberg, T. Hallam, J. J. Boland, J. J. Wang, J. F. Donegan, J. C. Grunlan, G. Moriarty, A. Shmeliov, R. J. Nicholls, J. M. Perkins, E. M. Grieveson, K. Theuwissen, D. W. McComb, P. D. Nellist, *Science* **2011**, *331*, 568; c) B. Radisavljevic, A. Radenovic, J. Brivio, V. Giacometti, A. Kis, *Nat. Nanotechnol.* **2011**, *6*, 147.

[17] a) K. Zhang, M. Q. Ye, A. J. Han, J. L. Yang, *J. Solid State Chem.* **2019**, *277*, 68; b) J. Q. Wang, L. Liu, S. L. Jiao, K. J. Ma, J. Lv, J. J. Yang, *Adv. Funct. Mater.* **2020**, *30*, 2002595.

[18] Y. Sun, W. Zhong, Y. Q. Wang, X. B. Xu, T. T. Wang, L. Q. Wu, Y. W. Du, *ACS Appl. Mater. Interfaces* **2017**, *9*, 34243.

[19] G. H. Xiang, M. Y. Chen, Z. W. Ni, Y. Shen, L. H. Xu, *RSC Adv.* **2021**, *11*, 20180.

[20] M. Q. Ning, P. H. Jiang, W. Ding, X. B. Zhu, G. G. Tan, Q. K. Man, J. B. Li, R. W. Li, *Adv. Funct. Mater.* **2021**, *31*, 2011229.

[21] M. Q. Ning, M. M. Lu, J. B. Li, Z. Chen, Y. K. Dou, C. Z. Wang, F. Rehman, M. S. Cao, H. B. Jin, *Nanoscale* **2015**, *7*, 15734.

[22] H. Q. Guo, L. Wang, W. B. You, L. T. Yang, X. Li, G. Y. Chen, Z. C. Wu, X. Qian, M. Wang, R. C. Che, *ACS Appl. Mater. Interfaces* **2020**, *12*, 16831.

[23] M. Q. Ning, Q. K. Man, G. G. Tan, Z. K. Lei, J. B. Li, R. W. Li, *ACS Appl. Mater. Interfaces* **2020**, *12*, 20785.

[24] W. D. Zhang, X. Zhang, Y. Zheng, C. Guo, M. Y. Yang, Z. Li, H. J. Wu, H. Qiu, H. X. Yan, S. H. Qi, *ACS Appl. Nano Mater.* **2018**, *1*, 5865.

[25] a) G. L. Di Benedetto, L. A. Morris, D. B. Swanson, B. D. Wightman, R. R. Carpenter, C. W. McMullan, R. M. Dratler, P. A. Sanchez, *J. Electrochem. Soc.* **2021**, *168*, 046520; b) Y. Luo, J. Y. Ding, Y. G. Shen, W. F. Tan, F. Liu, G. H. Qiu, *J. Soil. Sediment.* **2018**, *18*, 564.

[26] a) J. Zheng, R. Fan, H. Q. Wu, H. H. Yao, Y. J. Yan, J. M. Liu, L. Ran, Z. F. Sun, L. Z. Yi, L. Dang, P. P. Gan, P. Zheng, T. L. Yang, Y. Zhang, T. Tang, Y. Wang, *Nat. Commun.* **2019**, *10*, 1604; b) T. Li, P. L. Wang, W. B. Guo, X. M. Huang, X. H. Tian, G. R. Wu, B. Xu, F. F. Li, C. Yan, X. J. Liang, H. M. Lei, *ACS Nano* **2019**, *13*, 6770.

[27] a) S. Y. Wang, B. H. Chen, L. P. Ouyang, D. H. Wang, J. Tan, Y. Q. Qiao, S. F. Ge, J. Ruan, A. Zhuang, X. Y. Liu, R. B. Jia, *Adv. Sci.* **2021**, *8*, 2004721; b) H. P. Liu, J. F. Li, X. M. Liu, Z. Y. Li, Y. Zhang, Y. Q. Liang, Y. F. Zheng, S. L. Zhu, Z. D. Cui, S. L. Wu, *ACS Nano* **2021**, *15*, 18505.

[28] a) J. Li, S. Song, J. S. Meng, L. Tan, X. M. Liu, Y. F. Zheng, Z. Y. Li, K. W. K. Yeung, Z. D. Cui, Y. Q. Liang, S. L. Zhu, X. C. Zhang, S. L. Wu, *J. Am. Chem. Soc.* **2021**, *143*, 15427; b) Y. D. Xu, X. M. Liu, Y. F. Zheng, C. Y. Li, K. W. K. Yeung, Z. D. Cui, Y. Q. Liang, Z. Y. Li, S. L. Zhu, S. L. Wu, *Bioact. Mater.* **2021**, *6*, 1575.

[29] L. G. Jin, P. Hu, Y. Y. Wang, L. J. Wu, K. Qin, H. X. Cheng, S. H. Wang, B. X. Pan, H. B. Xin, W. H. Zhang, X. L. Wang, *Adv. Mater.* **2020**, *32*, 1906050.